Chapter 18
Dealloyed Pt-Based Core–Shell Catalysts for Oxygen Reduction

Lin Gan and Peter Strasser

Abstract In this chapter, we review recent works of dealloyed Pt core–shell catalysts, which are synthesized by selective removal of transition metals from a transition-metal-rich Pt alloys (e.g., PtM_3). The resulted dealloyed Pt catalysts represent very active materials for the oxygen reduction reaction (ORR) catalysis in terms of noble-metal-mass-normalized activity as well as their intrinsic area-specific activity. The mechanistic origin of the catalytic activity enhancement and the stability of dealloyed Pt catalysts are also discussed.

18.1 Introduction

As a highly efficient and clean energy conversion technology, polymer electrolyte membrane fuel cells (PEMFCs) have attracted substantial interests over the past few decades [1–4]. Prototype vehicles powered by fuel cells with impressive performance have been released by several manufactures, but it is still difficult to move to practical technique that can be mass-produced cost-effectively. One of the main obstacles is the slow rate of the cathodic oxygen reduction reaction (ORR), which currently relies on noble-metal Pt as the electrocatalysts. The high cost and limit resource of Pt force the urgent development of low-/non-Pt catalysts. Ideally, non-noble-metal catalyst is the best and ultimate goal. Unfortunately, although significant progress has been made in terms of the activities of noble-metal-free catalysts in recent years, their stability as well as the mass transport still needs further breakthroughs [5–8]. As a compromise, low-Pt catalyst appears to be a feasible way for the medium-term development of PEMFCs. In this direction, the United States Department of Energy (DOE) sets up a 2017 target on the total platinum group

L. Gan • P. Strasser (✉)
The Electrochemical Energy, Catalysis, and Materials Science Laboratory, Department of Chemistry, Chemical Engineering Division, Technical University Berlin, 10623 Berlin, Germany
e-mail: pstrasser@tu-berlin.de

M. Shao (ed.), *Electrocatalysis in Fuel Cells*, Lecture Notes in Energy 9,
DOI 10.1007/978-1-4471-4911-8_18,

metals (PGM) loading of 0.125 mg cm^{-2} on MEAs to achieve a power density of 8 kW g^{-1}_{Pt}. This corresponds to the use of 8 g of PGM per vehicle, which is comparable to what has been used in an internal combustion engine today [4]. To realize this target, the new ORR electrocatalyst must show a stable Pt-normalized mass activity of at least fourfold improvement compared with the state-of-the-art Pt catalyst.

Rational catalyst development to meet the activity target needs a comprehensive understanding of the ORR kinetics. This is why the ORR has been extensively studied for several decades. Regardless the mechanistic detail, it is proposed that the intermediate oxygenated species (such as $–OH_{ad}$) adsorbs on the Pt surface too strongly to be removed and results in high coverage ratio of the oxygenated species on the Pt surface, which become the main reason for the slow kinetics of ORR on Pt. It is therefore expected that a slightly weakened binding energy between the oxygenated species and Pt surface could result in a higher ORR activity. This could be realized by tailoring the electronic structure of Pt surface (particularly the d-band center), as predicted by density functional calculations [9–11].

From the late 1990s, Pt alloys containing a late 3d-transition metal "M" (M = Fe, Co, Ni, etc.) were found to be more catalytically active than pure Pt on ORR [1, 12–17]. The Pt alloys, mostly close to a stoichiometric ratio of Pt_3M, showed around twofold enhancement in the Pt-mass activity. Although their activities were far away from the DOE target, these pioneer studies provide important insights on the possible activity-enhancement mechanisms: (1) ligand effects, due to proximity of transition metals with different electron negativity and thus direct electron interaction, typically operative over one to three atomic layers, and (2) geometric effects associated with shortened nearest-neighboring Pt–Pt interatomic distances in the Pt alloys. Both of the two effects could induce the change of electronic structure of Pt surface and therefore weakened adsorption of intermediate oxygenated species.

Based on these guidelines, great progress on the structural design of Pt-based bimetallic/trimetallic catalysts has been made in past 10 years, as highlighted by several recent reviews [2–4]. For instance, the "Pt-monolayer catalysts" reported by Adzic and coworkers, which consist of a single Pt monolayer supported on non-Pt metal substrate (e.g., Pd) [11, 18–23], exhibited significant ORR activity enhancement based on Pt mass. Meanwhile, Stamenkovic et al. reported a class of highly active "Pt-skin catalysts," which were formed by surface segregation in Pt_3M alloys upon thermal annealing, resulting in a Pt monolayer on top of an M-enriched second layer [9, 24–26]. A common structural feature of the two classes of highly active catalysts is that a single Pt monolayer supported on the second layer containing a heteroatom, which could not only result in direct electron interaction with Pt but also a strain effect on the Pt monolayer caused by lattice mismatch. As a result, both ligand effect and geometric effect could contribute to their enhanced ORR activities.

In this chapter, we review dealloyed core–shell nanoparticle catalysts, which were synthesized by selective dissolution of transition metals from the surface of a transition-metal-rich Pt alloys (e.g., PtM_3). Figure 18.1 shows an illustration of the

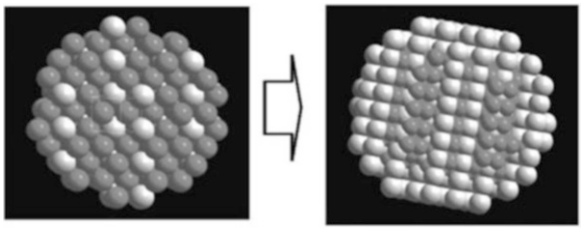

Fig. 18.1 Dealloying of $PtCu_3$ nanoparticles formed Cu-rich alloy core and Pt-rich shell (*gray*: Cu; *white*: Pt) (reprint with permission from ref. [27])

dealloyed core–shell nanoparticle concept, indicating the formation of a transition-metal-rich core and Pt-rich shell. We will show that the dealloyed core–shell nanoparticles represent very active materials for the ORR catalysis in terms of their noble-metal-mass-based ORR activity as well as their intrinsic specific activity. In contrast to the "Pt-skin" and the "Pt-monolayer" catalysts, the thickness of the Pt-enriched shell of the dealloyed catalysts is thicker than a single monolayer, which results in a dominate lattice-strain-controlled ORR activities of the dealloyed surfaces. The activities as well as the stability of the family of dealloyed Pt-based catalysts would be discussed in detail. Finally, we will discuss recent advances on the atomic-scale structural studies of the dealloyed core–shell nanoparticles, providing a deeper insight on their structure–activity–stability relationship.

18.2 A Historical View of Dealloying: From Bulk Materials to Nanoparticles

Dealloying, also called selective leaching, is a process where the less-noble metals are selectively dissolved out of an alloy and has been historically used in technologically important alloys in the context of corrosion area [28]. A most common example is the selective leaching of zinc from brass alloys (15 at% Zn) in the presence of oxygen and moisture, resulting in a copper-rich sponge with poor mechanical properties. In this situation, the dealloying process caused undesired performance decline and thus needs to be avoided, which continues to be a main task in corrosion area. Despite its negative effect in the corrosion area, dealloying can be useful in some certain areas regarding its ability to create porous structure. A well-known instance is the Raney nickel developed by Murray Raney more than 80 years ago [29], which was produced from a block of Ni–Al alloy treated with concentrated alkaline, dissolving most of Al out of the alloy and leaving behind a porous structure. The size of these pores was already in the nanoscale region, even though the concept of "nanotechnology" arises several decades later. The resulted nanoporous nickel-rich structure showed a high specific surface area, making it quite useful as heterogeneous catalysts in a variety of organic synthesis (e.g., hydrogenation reactions).

Inspired by the successful application of Raney nickel and also the arising of nanotechnology, there are increasing interests in synthesizing nanoporous materials

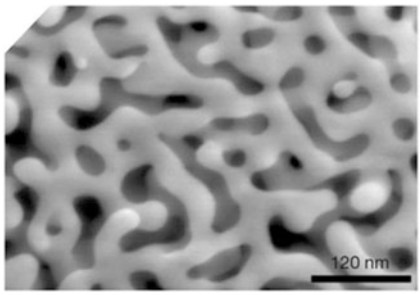

Fig. 18.2 Nanoporosity formed by dealloying of a bulk Ag–Au alloy (reprint with permission from ref. [30])

using dealloying protocol for applications in catalysis and sensors in recent years [30–35]. For example, nanoporous gold (Fig. 18.2) was synthesized by electrochemical dealloying of silver–gold alloy. Other nanoporous materials, such as Pt and Pd, were also synthesized.

The dynamic process of dealloying was discussed using Monte Carlo simulations [30, 36, 37]. The dissolution of the less-noble atoms from the topmost surface resulted in steps and kinks, where the coordinated numbers of noble atoms increased. This induced a surface diffusion of noble atoms. The competition between the dissolution rate of less-noble metals and the surface diffusion of noble metals is considered to be a key factor that controls the morphology of the dealloyed product. In bulk alloys, surface diffusion rate of the noble atoms is slow across the extended surface, which causes a Rayleigh surface instability [37] and leads to the formation of nanoporosity.

Until recently, all dealloying processes are studied in bulk alloy materials with the aim to produce nanoporosity. From 2007 on, we applied and studied the dealloying process in real engineered fuel cell Pt–M alloy nanoparticle catalysts. Unlike macro bulk materials, dealloying of alloy nanoparticles with small enough particle size produces solid core–shell nanoparticles. This may be due to the fact that the residual Pt atoms on the nanoparticles exhibited lower average coordination and hence experienced a much faster surface diffusion compared to those on the bulk surface. We will show that, using transition-metal-rich Pt alloy precursors, the dealloyed nanoparticle catalyst can produce up to eightfold enhancement in the Pt-mass-normalized ORR activity due to an enhanced lattice-strain effect.

18.3 Dealloyed Pt-Bimetallic Nanoparticle Catalysts

18.3.1 Dealloyed $PtCu_3$ Catalysts: Synthesis and Activities

The synthesis of dealloyed $PtCu_3$ catalyst involved the preparation of $PtCu_3$ precursor alloys at the first step, which was followed by electrochemical dissolution of Cu (dealloying). $PtCu_3$ alloy precursors were prepared by a conventional

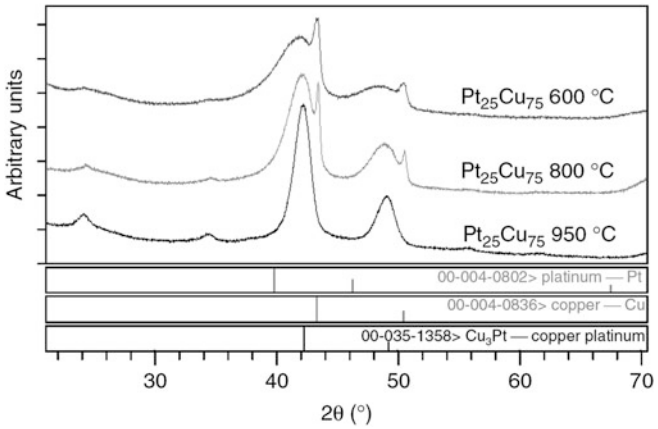

Fig. 18.3 XRD patterns of $Pt_{25}Cu_{75}$ precursor alloys annealed at different temperatures (reprint with permission from ref. [27])

impregnation-reductive annealing method. Normally, a carbon-supported Pt catalyst was impregnated with Cu salt at a desired atomic ratio between Pt and Cu firstly, which was further annealed by H_2 at elevated temperatures to reduce Cu and promote the alloying of Cu with Pt.

Figure 18.3 shows the XRD patterns of $PtCu_3$ catalyst annealed at 600, 800, and 950 °C and also the standard diffraction peaks of pure Pt and Cu for comparison [27]. The {111} diffraction peak position is located between the Pt {111} peak and Cu {111} peak, indicating a smaller lattice parameter of the alloy compared to pure Pt. The higher annealing temperature resulted in a more uniform alloy from multiphase (Pt-rich and Cu-rich alloys) to single phase, while the average crystal size evaluated from the full width at half maximum (FWHM) increased due to particle sintering at higher temperatures. The maximum annealing temperature essentially controlled the Cu content of the resulting disordered Pt–Cu lattices, while increasing annealing times, in contrast, leads primarily to particle growth [38, 39]. Correlation of annealing control parameters, such as heating rate, temperature, and time, with microscopic alloy structure, composition, and particle size has also been studied in situ by using high-temperature XRD [39].

The subsequent dissolution (dealloying) of Cu is the key process to form the active catalyst. Briefly, the dealloying can be performed by chemical leaching in acid solution (HNO_3 for Cu) or in an electrochemical way. One benefit of the electrochemical dealloying is its ability to in situ monitoring the dissolution of Cu. Figure 18.4a shows the initial three cyclic voltammograms (CV) of the dealloying of $PtCu_3$ catalyst annealed at 600 °C. Normally, there is a characteristic underpotential adsorption/desorption peak of H (H_{upd}) on a Pt electrode between 0.05 and 0.4 V/RHE as demonstrated on the commercial Pt catalyst in Fig. 18.4a. However, in the very first Pt–Cu dealloying CV, no H_{upd} peak could be found, consistent with complete Cu surface segregation in Cu-rich Pt alloys. Sweeping

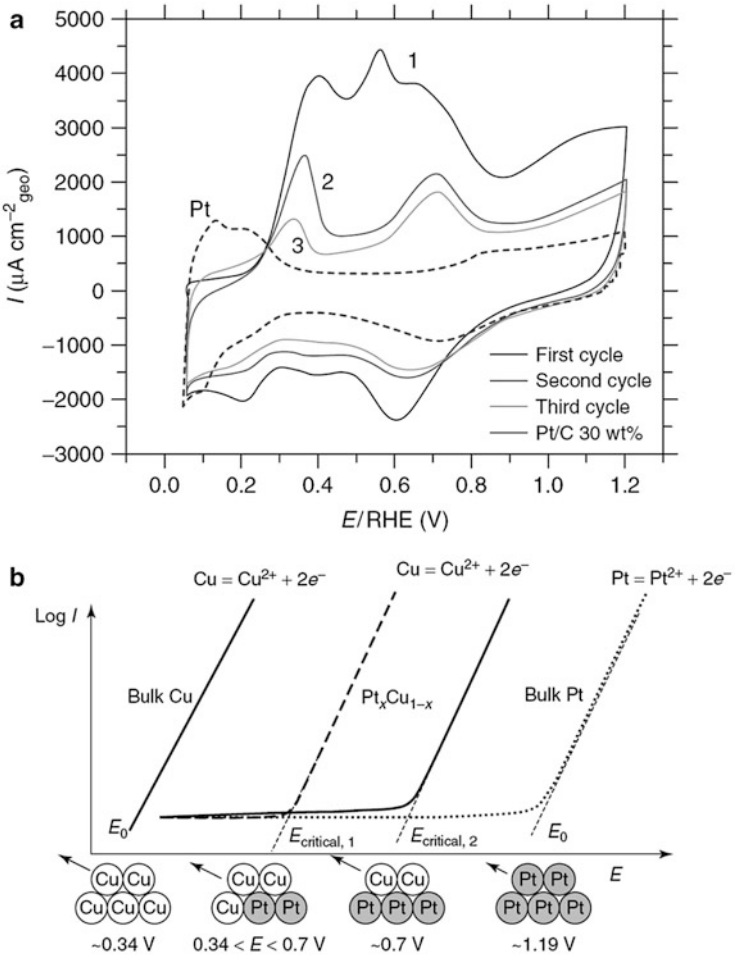

Fig. 18.4 (**a**) Initial three CVs of the $PtCu_3$ catalyst annealed at 600 °C during electrochemical dealloying compared to the CV of a commercial Pt catalyst (reprint with permission from ref. [27]). (**b**) Diagrammatic illustration of how the critical dissolution potential of a Cu monolayer depends on the composition of its subsurface layer (reprint with permission from ref. [40])

anodically, a broad peak from 0.3 to 0.85 V arises corresponding to the Cu dissolution, in which several fine sub-peaks can be resolved. A detailed description of these fine peaks was performed by density functional calculations, suggesting the dissolution of Cu at different surface sites, as shown in Fig. 18.4b [40]. On the second and the third cycle, additional anodic Cu dissolution peaks can be still seen but decreased gradually in intensity, while the H_{upd} features gradually emerged, indicating exposure of Pt atoms on the surface.

After 200 cycles of electrochemical dealloying, the Cu dissolution vanished completely and the CV for all the dealloyed $PtCu_3$ catalysts exhibited stable Pt-like

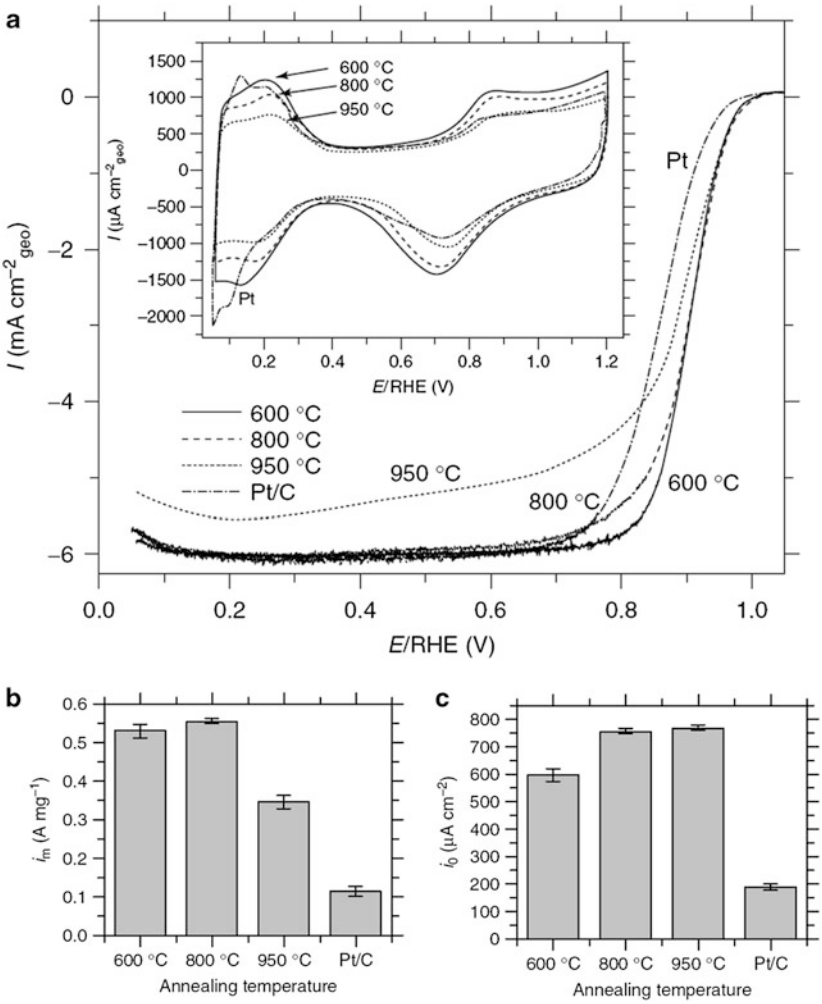

Fig. 18.5 (**a**) ORR voltammetry in O_2-saturated 0.1 M $HClO_4$ of dealloyed PtCu3 catalysts using the alloy precursors annealed at 600, 800, and 950 compared to a commercial Pt catalyst. (*Inset*) CV curves of the dealloyed PtCu3 catalysts in N_2 saturated 0.1 M $HClO_4$. (**b**) Comparison of Pt-mass activities at 0.9 V/RHE. (**c**) Comparison of Pt-area-specific activities at 0.9 V/RHE (reprint with permission from ref. [27])

feature (as shown in the inset of Fig. 18.5a). The resulted dealloyed "$PtCu_3$" catalysts showed very high catalytic activities in the ORR measurements (Fig. 18.5a), producing previously unachieved 3–5-fold improvement on the Pt-mass activity (Fig. 18.5b) and 3–4-fold on the Pt-area-specific activity (Fig. 18.5c) over pure Pt at 0.9 V vs. RHE. The highest Pt-mass activity (0.56 A mg^{-1}_{Pt}) was achieved on the dealloyed $PtCu_3$ catalyst using the precursor annealed at 800 °C, which obviously exceeded the DOE 2017 activity target (0.44 mg^{-1}_{Pt}). This fivefold activity enhancement would

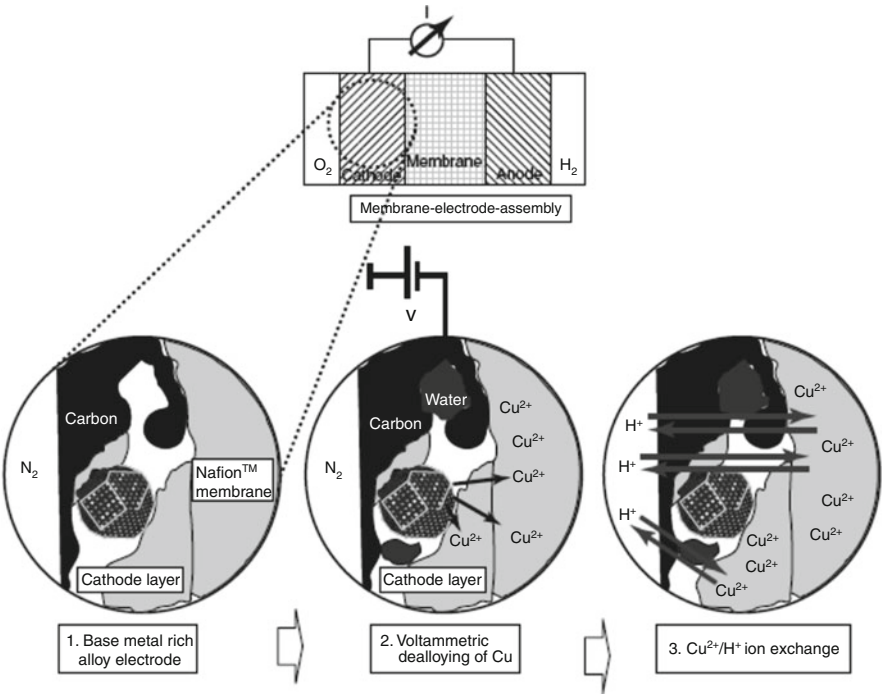

Fig. 18.6 A novel three-step method for in situ electrochemical dealloying of transition-metal-rich Pt alloy catalyst inside MEA (reprint with permission from ref. [41])

correspond to 80 % reduction on the Pt usage, thus providing a promising route for the development of low-Pt fuel cell catalysts. This study demonstrates that electrochemical dealloying of non-noble base metals from base-metal-rich Pt-bimetallic alloys significantly alters the catalytic rates of the resulting Pt shells.

The practical usefulness of a novel ORR electrocatalyst depends on the feasibility to incorporate it into a realistic MEA and a single fuel cell. For this purpose, we developed a novel three-step method to implement in situ electrochemically dealloyed $PtCu_3$ ORR catalysts inside the MEA [38, 41], as schematically illustrated by Fig. 18.6. In step 1, the Cu-rich alloy precursor is incorporated in the cathode of a fuel cell. During step 2, a CV treatment is applied to the fuel cell, which results in the in situ dissolution of Cu atoms from the alloy particle surface. The dissolved Cu ions would diffuse into the Nafion polyelectrolyte and get trapped at negatively charged sulfonic acid groups of the latter, which is detrimental to the ion conductivity and result in decreased fuel cell performance. As a result, an ion-exchange step (step 3) is needed, where the MEA is treated with an inorganic acid to completely exchange the trapped Cu ions with protons from the liquid acid. After the three steps, the catalyst has been converted into its active state and is ready for use.

18.3.2 Mechanism of Activity Enhancement: Lattice-Strain Effect

Unlike Pt-monolayer catalysts and Pt-skin catalysts, the dealloyed $PtCu_3$ catalysts consist of a pure Pt shell with several atomic layers. The near-surface content of Cu was very low. The thickness of the Pt shell can be clearly imaged by scanning transmission electron microscopy (STEM) and energy-dispersive X-ray spectroscopy (EDX) line profiles (Fig. 18.7a, b). In the Z-contrast STEM image, the dealloyed particles show a brighter shell relative to a darker core, indicating the formation of Pt-rich shell. From the EDX line profiles, the thickness of the Pt-rich shell can be determined to be around 0.6 nm (corresponding to ca. 3 atomic layers). This result is consistent with the anomalous small-angle X-ray scattering (ASAXS) studies, which revealed a minimum Pt-shell thickness of 0.5 nm [42]. Across the Pt shell with a thickness of three atomic layers, a significant electronic interaction between the Cu atoms at the core and the outmost Pt surface is unlikely. Instead, the structural arrangement of Pt atoms on the surface with its shorter than normal Pt–Pt distance is creating a compressive-strain effect. This arises because of a lattice mismatch between the Pt shell and the Cu-rich alloy core. The compressive lattice strain changes the electronic properties of Pt and the adsorption on oxygenated species and thus accounts for the observed enhanced ORR activity.

To investigate the possible lattice-strain mechanism on the enhanced ORR activities, we synthesized two sets of dealloyed $Pt_{1-x}Cu_x$ catalysts from a wide range of alloy precursor compositions (Pt_3Cu, PtCu, and $PtCu_3$); one set was annealed at 800 °C and the other set annealed at 950 °C [43]. The idea is that the composition of the alloy core determines the upper limit of the strain on the Pt shell and thus enables a lattice-strain control, which is crucial for the study of strain–activity relationships.

The lattice strain in the Pt shell can be quantitatively estimated by anomalous X-ray diffraction (AXRD) analysis using a simple two-phase model (Fig. 18.7c), i.e., a Pt–Cu alloy core and a uniformly strained Pt shell. Figure 18.7d shows the measured average lattice parameters of the Pt shells (a_{shell}) as a function of precursor composition and preparation temperature. As expected, for all the dealloyed catalysts, a_{shell} is smaller than that of pure Pt (dotted line, Fig. 18.7d), indicating a compressive strain in the Pt shells. Increasing Cu in the alloy precursor or with a higher preparation temperature resulted in a decreased a_{shell} and hence a larger magnitude of the compressive strain. This can be well understood based on the core–shell model. That is, the lattice mismatch between the Pt shell and the Pt–Cu core causes a reduced Pt–Pt distance in the shell; the richer in Cu the particle core is, the smaller the lattice parameter and hence the higher the compressive strain induced in the shell. Similarly, in the high-temperature material, the bimetallic precursor phase is alloyed more uniformly with less residual, unalloyed Cu, which effectively makes the alloy phase richer in Cu.

To mimic the structural and electronic environment of the Pt layers surrounding a particle core with smaller lattice parameters in the dealloyed Pt–Cu catalysts, we extended and applied these ideas to bimetallic single-crystal model surfaces that consist of Pt overlayers with various thicknesses grown on a Cu(111) substrate.

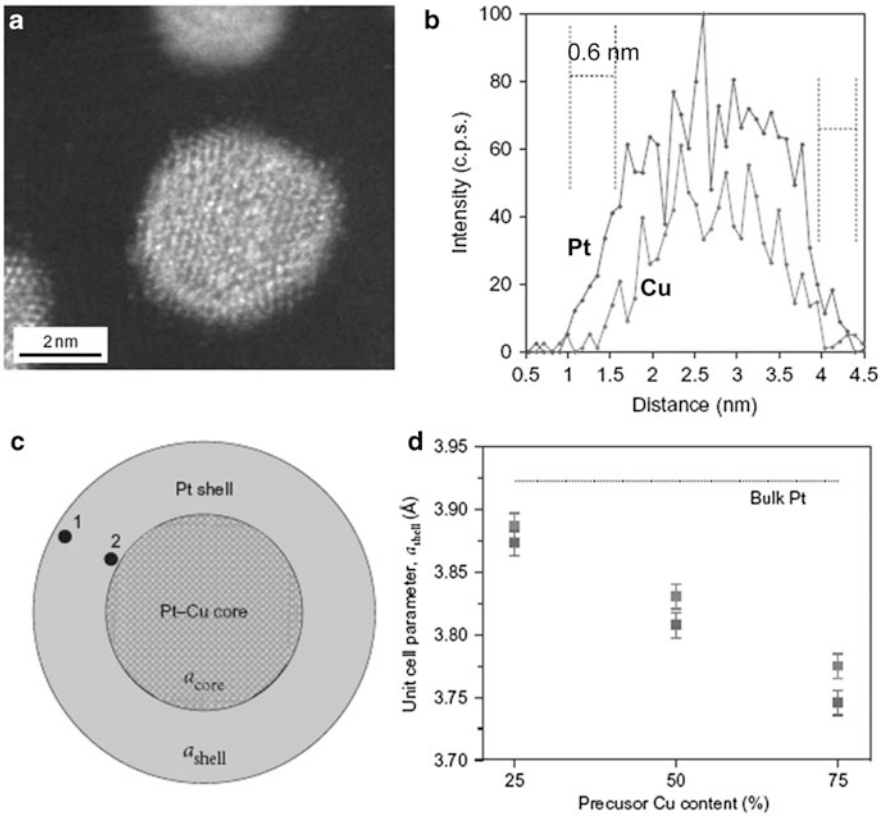

Fig. 18.7 (**a**) HAADF-STEM image of the dealloyed PtCu3 nanoparticle, showing an outer Pt-enriched shell (which images *brightly*) and a Cu-rich alloy core (which images *less brightly* than the shell). Contrast variations in the HAADF-STEM images relate to the atomic number (Z) difference between Pt and Cu, i.e., the so-called Z-contrast imaging. (**b**) EDX line profile across an individual dealloyed $PtCu_3$ nanoparticle acquired using a probe-corrected STEM with a probe size of ~0.2 nm. The thickness of the Pt-enriched shell was determined to be ~0.6 nm as shown by the *dash lines*. (**c**) A simple structural two-phase core–shell model for the dealloyed nanoparticle, i.e., pure Pt layers, surrounds an alloy particle core, where a_{shell} and a_{core} represent the average lattice parameters in shell and core, respectively. (**d**) Determination of a_{shell} as a function of the Cu content in the precursors annealed at 950 °C (*bottom*) and 800 °C (*top*). All alloys show Pt shells with lattice parameters below that of pure bulk Pt (*dotted line*) (reprint with permission from ref. [43])

The strain in the deposited platinum layers was measured by low-energy electron diffraction (LEED), as shown in Fig. 18.8a. An increase of the thickness of Pt layers resulted in decreased strain, indicating that the strain was relaxing in the Pt layers. Meanwhile, we have used X-ray emission spectroscopy (XES) and X-ray adsorption spectroscopy (XAS) to probe the occupied and unoccupied portion of the Pt-projected d bands, as illustrated in Fig. 18.8b. The sketch of Fig. 18.8c on left

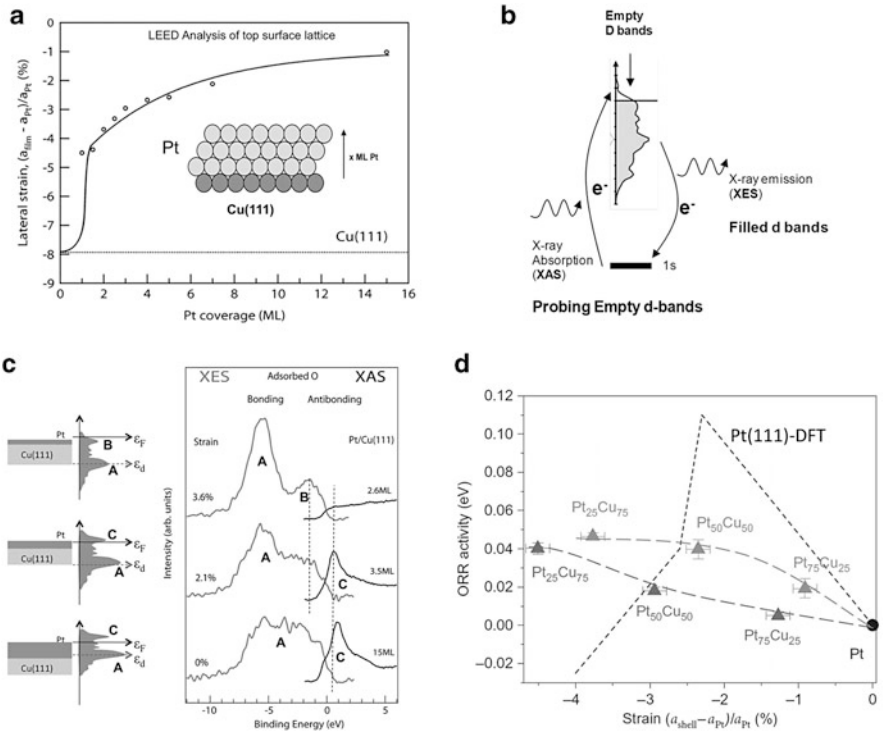

Fig. 18.8 (**a**) Compressive strains in Pt overlayers deposited on Cu (111), deduced from LEED patterns as a function of film thickness. (**b**) An illustration of probing the occupied and unoccupied portion of the Pt-projected d bands by using XES and XAS, respectively. (**c**) In-plane polarized oxygen K-edge XAS and normal emission oxygen K-edge XES of 0.2 ML of oxygen chemisorbed on Pt layers on Cu(111) with different thickness. (**d**) Experimental and predicted relationships between ORR activity and lattice strain in units of $kT{\cdot}\ln(j_{s,alloy}/j_{s,Pt})$, $T = 298$ K. The experimental ORR activities of the two families of dealloyed Pt–Cu nanoparticles (precursors prepared at 850 °C (*top*) and 900 °C (*bottom*)) are plotted as a function of strain in the particle shell (*dash lines* are to guide the eye). The *short dashed line* is the DFT-predicted volcano-shaped trend of the ORR activity for a Pt(111) single-crystal slab under isotropic strain. Moderate compressive lattice strain is predicted to enhance the rate of ORR catalysis (reprint with permission from ref. [43])

indicates three different thicknesses of the Pt overlayer (shell) on the Cu substrate (core). The sketches of the d bands on left stem from density functional calculation (DFT) predictions. The experimental XES and XAS results show that as the shell becomes thinner (top case), unoccupied states (still visible in XAS in bottom experiment) become occupied (top experiment) and thus show up in the XES curve rather than in the XAS curve, leading to a downward shift of the Pt d-band center.

Nørskov and coworkers have successfully developed a d-band theory in relating the adsorption properties of rate-limiting intermediates in catalytic process to electronic structure of catalyst surfaces [44, 45]. According to this theory, the

valence p-level of the ORR intermediate adsorbate (O/OH) forms bonding and antibonding states with the Pt d-band. Population of any antibonding state would lead to Pauli repulsion, and the Pt–O bond strength would be thereby weakened. A downward shift of the Pt d-band pulls more of the antibonding states below the Fermi level, which results in increasing occupation and weaker adsorbate bonding [9]. To understand the relationship between surface strain, Pt–O binding energy, and the catalytic ORR reactivity, we further carried out DFT calculations for a strained Pt(111) model surface (the dashed line in Fig. 18.8d). The DFT calculations derived a "volcano" relation between the predicted ORR rate and the strain, implying that compressive strain first enhances the overall ORR activity by reducing the binding energy of intermediate oxygenated adsorbate and, thereby, lowers the activation barriers for proton- and electron-transfer processes. Beyond a critical strain, however, the binding becomes too weak, and the catalytic activity is predicted to decrease because of an increased activation barrier for either oxygen dissociation or the formation of oxygenated intermediate.

Correlating the experimental synthesis–strain–activity data of the two sets of dealloyed core–shell nanoparticles (Fig. 18.8d), we provide the experimental evidence that the deviation of the Pt-shell lattice parameter from that of bulk Pt, i.e., the lattice strain in the shell, is the controlling factor in the catalytic enhancement of dealloyed Pt nanoparticles. In each set of dealloyed Pt–Cu catalysts, it is unambiguously confirmed that a moderate increase of the compressive strain in the Pt shell resulted in a higher ORR activities, which correlates well with our DFT predictions. Nevertheless, we did not observe a decrease in the experimental activity values on the left side of the volcano curve, as predicted by the DFT calculations. This is related to compressive-strain relaxation in the Pt shells, which prevent the buildup of high strain energy. Pt atoms adjacent to the Pt–Cu cores (Fig. 18.7c, point 2) adopt a lattice parameter closer to that of the cores, but outer Pt-shell atoms (Fig. 18.7c, point 1) relax toward the lattice constant of bulk Pt. Hence, the real surface strain is less than a_{shell}, which is an average strain in the Pt shell; if the real surface strain was plotted in Fig. 18.8d, we would expect a shift of all experimental data points to the right. Figure 18.8d also reveals that the set of dealloyed nanoparticle catalysts prepared at the higher annealing temperature exhibits reduced activity at comparable lattice strain in the particle shells, presumably because of differences in the mean particle size. Hence, our strain-related conclusion generally refers to particles of comparable size.

18.3.3 Extension to Other Dealloyed Transition-Metal-Rich Pt-Bimetallic Catalysts

The dealloyed core–shell nanoparticle concept revealed in the dealloyed Pt–Cu catalysts can be generalized in a broad range of transition-metal-rich Pt-bimetallic

catalysts such as Pt–Co, Pt–Ni, and Pt–Fe alloys. As suitable candidates for the ORR catalysts, these Pt-bimetallic alloys have been extensively investigated during the past years, and most of these studies were focused on a stoichiometry of around Pt_3M [1, 12–14, 46].

Mani et al. [47] reported a comparative study of different dealloyed Pt binary PtM_3 (M = Cu, Co, and Ni) catalysts for use in PEMFC cathode. All the catalysts were prepared by impregnation and followed annealing protocol, after which they were implemented in single fuel cell MEA and activated by in situ electrochemical dealloying. The dealloyed binary PtM_3 catalysts showed more than a threefold improvement for M = Co, Cu and close to a threefold improvement for M = Ni in terms of Pt-mass activity of the single fuel cell compared to a 45 wt% Pt/C reference cathode catalyst. An overview of the Pt-mass ORR activities reported in further reports suggests an order of dealloyed $PtCu_3$ > dealloyed $PtCo_3$ > dealloyed $PtNi_3$ [47–50]. Nevertheless, the synthesis based on the impregnation and annealing used here generally resulted in nanoparticles with a broad size distribution and different alloy degrees, which make direct result explanation difficult. Further studies in preparing homogenous nanoparticles are therefore needed to clarify the effect of different transition metals (Fig. 18.9).

The enhanced ORR activities of the dealloyed Pt binary catalysts could be related to a similar lattice-strain effect as revealed in the dealloyed $PtCu_3$ catalysts. However, it is still unclear what the origin of the different activities of different dealloyed PtM_3 catalysts is. Regarding their comparable atomic radius, the alloy elements Co, Ni, and Cu are assumed to induce a similar extent of lattice strain. Nevertheless, due to different redox chemistry of the transition metals, different extent of metal dissolution may exist [47], which might result in different core–shell fine structures and hence different activities.

The advantage of using transition-metal-rich alloys was further demonstrated by composition-dependent activity studies. In a series of Pt_3Co, PtCo, and $PtCo_3$, a maximum Pt-mass activity was observed in dealloyed $PtCo_3$ catalyst in O_2-saturated $HClO_4$ solution [51]. By preparation of monodisperse single-phase $Pt_{1-x}Ni_x$ catalysts, a ORR activity maximum was also uncovered at initial Ni content in the range of 70–75 at% [52, 53]. These results are consistent with the reports in dealloyed thin-film catalysts by researchers at 3M company, where a maximum ORR activity was observed in dealloyed $Pt_{1-x}Co_x$ catalyst with $x = 0.66–0.67$ and in dealloyed $Pt_{1-x}Ni_x$ catalyst with $x = 0.69$ [54, 55]. Nevertheless, there is discrepancy on the optimized initial composition in several other reports, where the highest ORR mass activity was found to be at a lower transition-metal content around 50 at% (e.g., $Pt_{50}Ni_{50}$ in both $Pt_{1-x}Ni_x$ nanoparticles [56] and $Pt_{1-x}Ni_x$ thin-film catalysts [57]). This discrepancy may possibly originate from different structure of precursor alloy catalyst (such as particle size and alloying degree) and also different dealloying protocols.

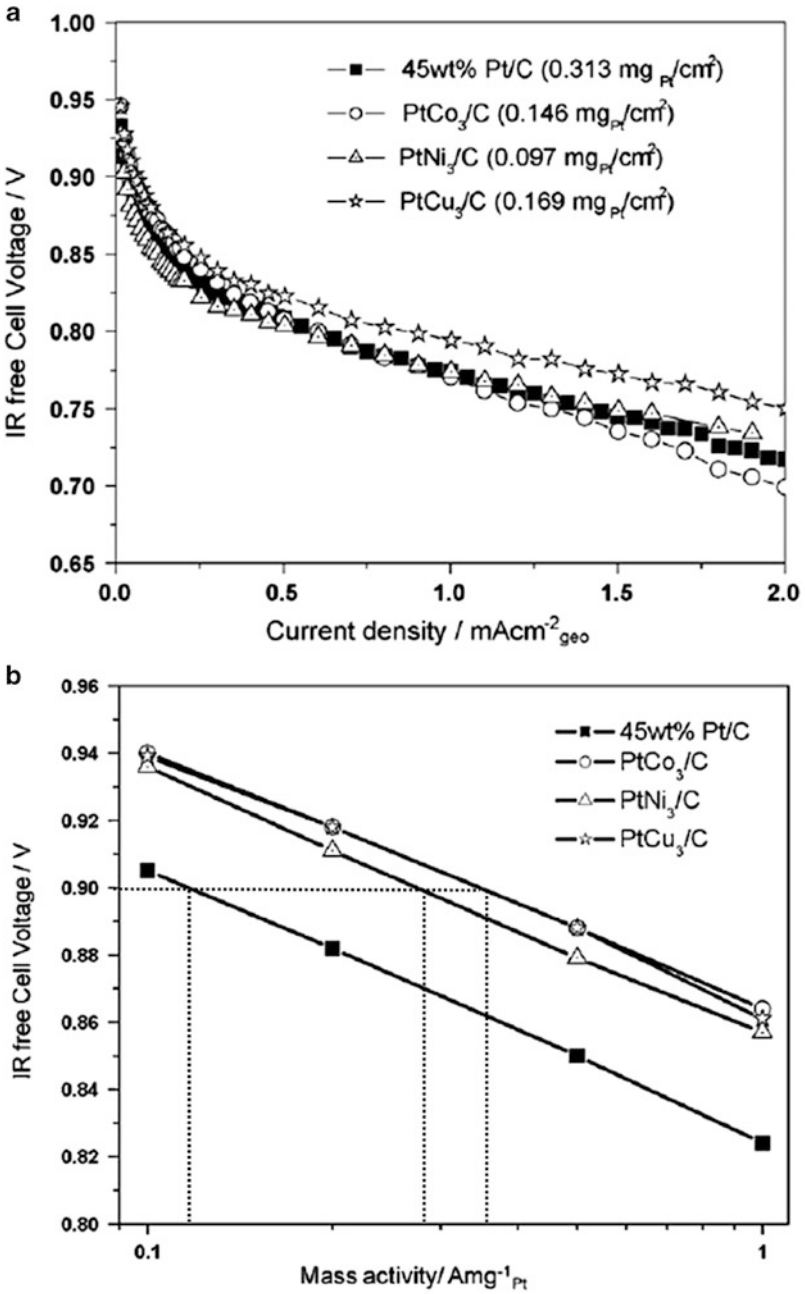

Fig. 18.9 (**a**) Current–voltage characteristics of 10 cm^2 single H_2/O_2 fuel cells using dealloyed $PtCu_3$, dealloyed $PtNi_3$, and dealloyed $PtCo_3$ cathode catalyst, in comparison with standard Pt cathode catalysts. (**b**) Pt-mass activities at 0.9 V of the dealloyed Pt-bimetallic cathode catalysts (reprint with permission from ref. [47])

18.4 Dealloyed Pt-Based Ternary Nanoparticle Catalysts

By introducing a third kind of transition-metal element, Pt ternary alloy catalysts attract considerable interests since the possibility of fine-tuning the geometric/electronic structures for further improved catalytic activity [58, 59]. Here, we show that the dealloying concept can be further applied in Pt ternary alloy catalysts, demonstrating a powerful approach to optimize the structure and activities of Pt alloy catalysts.

Figure 18.10 shows the ORR activities of dealloyed Pt–Cu–Co ternary catalysts with different Cu/Co compositions measured on a single 10 cm^2 single H_2/O_2 fuel cell [41]. The polarization curves for all the ternary catalysts shifted to more positive potentials compared to Pt catalyst, indicating lower overpotentials and hence higher catalytic activities. The dealloyed $Pt_{20}Cu_{20}Co_{60}$ exhibited unprecedented ORR activities of up to 0.5 A mg^{-1}_{Pt}, substantially surpassing the technological Pt-mass activity target in fuel cells (0.44 A mg^{-1}_{Pt}). The synergy between Co and Cu can be revealed by improved mass activity of dealloyed $Pt_{20}Cu_{20}Co_{60}$ compared to both dealloyed $PtCo_3$ and dealloyed $PtCu_3$ in the fuel cell test [41, 47]. Similar activity improvements were also reported in dealloyed $Pt_{20}Ni_{60}Cu_{20}$, $Pt_{20}Ni_{60}Fe_{20}$ and $Pt_{20}Ni_{60}Co_{20}$ catalyst compared to dealloyed $PtNi_3$ catalysts [47].

In principle, a similar compressive lattice-strain effect as revealed in the dealloyed Pt binary catalysts could also account for the higher activity of dealloyed Pt ternary catalysts compared with the pure Pt catalysts. Nevertheless, the origin of the activity enhancement for dealloyed ternary catalyst compared to the dealloyed Pt binary catalysts is still far from well understood. Exactly what kind of roles that the third element plays needs further studies.

18.5 Stability of Dealloyed Pt-Based Nanoparticle Catalysts

Stability is a critical criterion with the same importance as activity for the viability of an ORR catalyst in practical fuel cells. Since the ORR potential at the cathode of PEMFCs is up to 1.2 V, a carbon-supported Pt nanoparticle catalyst can exhibit several degradation mechanisms: (1) Ostwald ripening associated with Pt dissolution/redeposition, (2) particle migration and coalescence, and (3) carbon corrosion [60]. For Pt alloy catalysts, dissolution of non-noble element at high potentials becomes an additional mechanism for the catalyst instability. Dealloyed core–shell nanoparticles with protective Pt shells are assumed to be stable against further degradation associated with the dissolution of non-noble element. However, Mayrhofer and coworkers found that there was a surface segregation of the oxophilic non-noble metals initiated by the adsorption of oxygenated species (such as OH_{ad}) under the reactive conditions [61]. Such adsorption-induced surface segregation

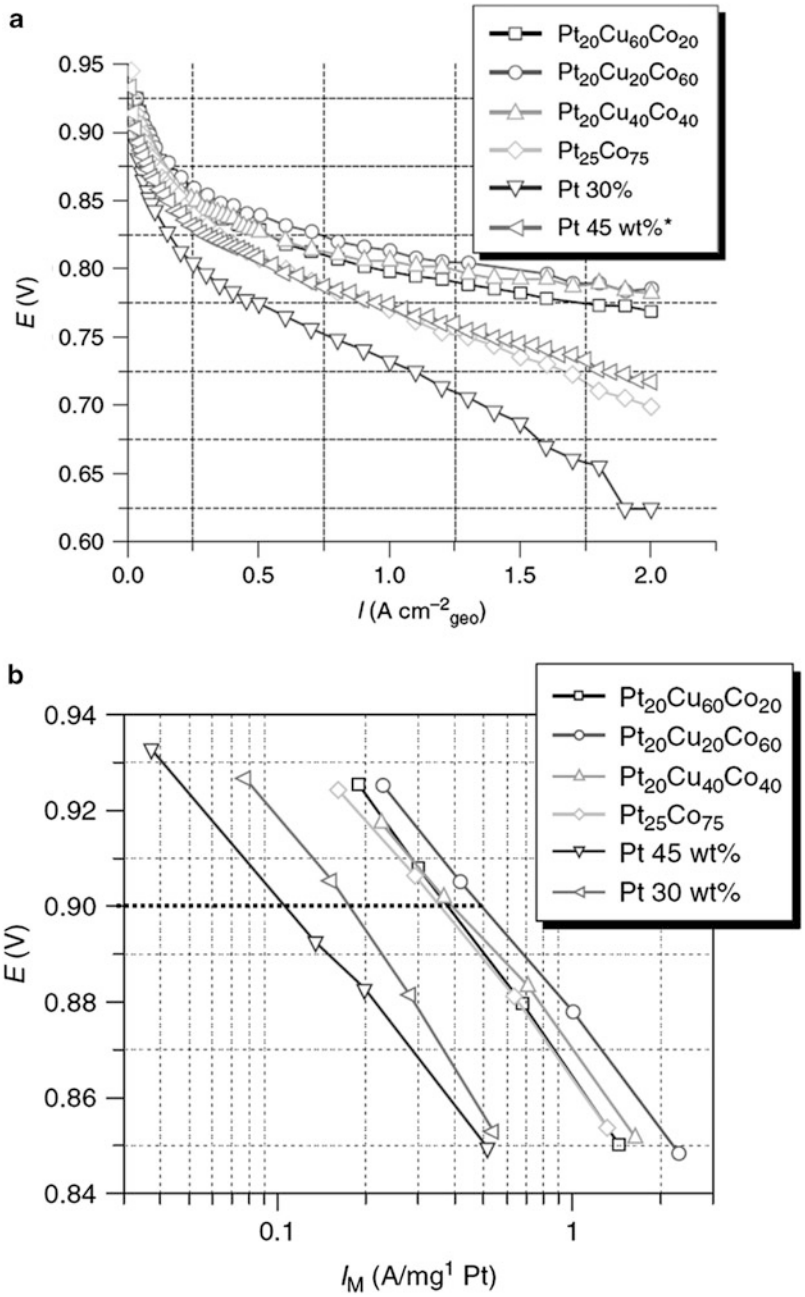

Fig. 18.10 (**a**) Current–voltage characteristics of 10 cm^2 single H_2/O_2 fuel cells using dealloyed Pt–Co–Cu cathode catalyst, in comparison with dealloyed $PtCo_3$ cathode catalyst and standard Pt cathode catalysts. (**b**) Pt-mass activities at 0.9 V of the dealloyed Pt–Co–Cu cathode catalysts (reprint with permission from ref. [41])

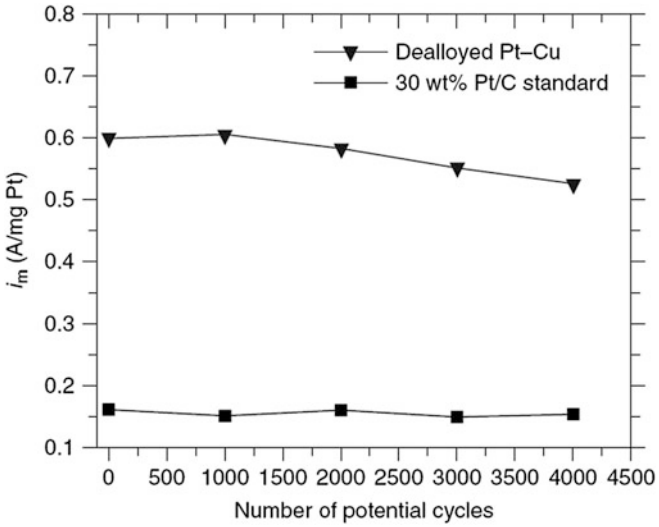

Fig. 18.11 Stability test of a dealloyed $PtCu_3$ catalyst prepared at 600 °C by potential cycles between 0.6 and 1 V/RHE in oxygen-saturated 0.1 M $HClO_4$ (100 mV s^{-1}) (reprint with permission from ref. [27])

would result in continued dissolution of the non-noble metals, which is detrimental to the stability of the particle-core composition and hence the lattice-strain-controlled ORR activities of the dealloyed Pt catalysts.

Figure 18.11 presents the evolution of the mass activity of a dealloyed $PtCu_3$ catalyst during 4,000 potential cycles between 0.6 and 1.0 V/RHE at 100 mV s^{-1}, indicating that it is able to maintain the activity enhancement over the Pt benchmark for a long period [27]. Nevertheless, continued degradation of the catalytic activity of dealloyed $PtCu_3$ is clearly shown.

The influence of different non-noble alloy component (e.g., Cu, Co, Ni, Fe) on the catalyst stability has not been well addressed until now. In a recent study, the specific activity of dealloyed $PtCu_3$ decreased 24 % after 10,000 cycles between 0.5 and 1.0 V while that decreased 42 % for dealloyed $PtCo_3$ [48]. The loss of Cu/Co in the catalysts was confirmed by compositional analysis using EDX. In comparison, dealloyed $PtNi_3$ showed 50 % decrease in the specific activity after the same test protocol [50]. It therefore seems that the stability of the different catalysts is in the order of dealloyed $PtCu_3$ > dealloyed $PtCo_3$ > dealloyed $PtNi_3$ [50]. This difference is likely due to the different redox chemistry or different Pt–M interactions of different alloy elements, but further systematic studies are needed to verify this hypothesis.

We also investigated the stability of dealloyed $Pt_{25}Cu_{75}$ and dealloyed $Pt_{20}Cu_{20}Co_{60}$ catalysts in a realistic fuel cell MEA operated at 80 °C by voltage cycling from 0.5 to 1.0 V at 100 mV s^{-1} (Fig. 18.12) [62]. After 30,000 voltage cycles, both dealloyed $Pt_{25}Cu_{75}$ and dealloyed $Pt_{20}Cu_{20}Co_{60}$ were able to retain their mass and specific activity advantage relative to Pt/C. The mass activity of the

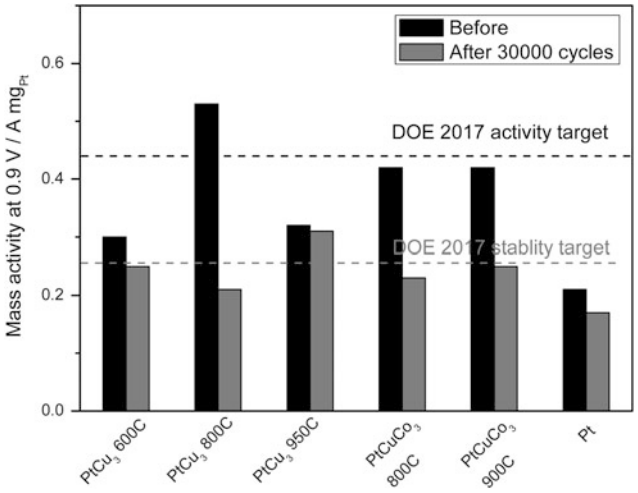

Fig. 18.12 Stability measurement of various dealloyed $PtCu_3$ and dealloyed $PtCuCo_3$ catalyst compared to pure Pt standard cathode catalysts in single fuel cell MEAs. The Pt-mass activities at 0.9 V are plotted before and after 30,000 voltage cycles (0.5–1.0 V, 100mV s^{-1}). Cell conditions: anode H_2/cathode N_2, 100 % relative humidity, 80 °C (reprint with permission from ref. [62])

dealloyed $Pt_{25}Cu_{75}$ prepared at 950 °C was even almost unchanged. Attractively, dealloyed $PtCuCo_3$ almost fulfilled both the DOE activity and stability target of 2017 (the dash lines in Fig. 18.12), which again highlights the benefit of dealloyed ternary catalysts compared to binary catalysts. Nevertheless, there is a disadvantage for Cu-containing catalysts that, once Cu was leached out, it can diffuse to and redeposit on the anode side, which would cause continuous performance loss of the anode side during long-term operation. Further optimization of the composition and structure of a wide range of ternary catalysts is currently underway.

18.6 Core–Shell Fine Structures: Understanding the Structure–Activity–Durability Relationships at Nano-/Atomic Scale

So far, we have presented several types of dealloyed Pt binary and ternary nanoparticle catalysts, which showed substantially enhanced ORR activities compared with pure Pt. The activity enhancement originated from a lattice-strain-controlled mechanism. However, it is still unclear why different transition metals resulted in different activities and stabilities and how particle structural characteristics such as size, shape, and composition would come into play. To understand these issues, it is important to achieve an atomic-scale understanding of the core–shell fine structures

of the dealloyed nanoparticles, i.e., Pt-shell thickness as well as compositional profile across the particle core, which play a critical role in the lattice-strain-controlled ORR activities.

The core–shell structure character of dealloyed Pt catalysts has been disclosed by various techniques such as anomalous X-ray diffraction [43], small-angle X-ray scattering [42], X-ray photoelectron spectroscopy [27, 43], and TEM/STEM [43, 63–69]. Among them, TEM/STEM is an indispensable tool for characterization at nano-/atomic scale in real space. In particular, the recently developed aberration-corrected TEM [70, 71] provides significantly improved spatial resolution down to sub-Ångstrom scale. Due to much decreased contrast delocalization and hence high accuracy on surface atomic structures, direct evidence of a gradient compressive strain on the Pt-rich shell was provided using aberration-corrected high-resolution TEM [67]. Meanwhile, combined with spectroscopic techniques such as energy-dispersive X-ray spectra (EDX) and electron energy loss spectroscopy (EELS), the convergent electron beam in the probe-corrected STEM becomes a powerful tool in revealing the compositional distribution in individual nanoparticles at atomic scale. Thanks to this advance, core–shell fine structures of the dealloyed nanoparticles were revealed at atomic scale, enabling a comprehensive understanding of the structure–activity relationships [23, 53, 63–66, 68, 69, 72, 73].

18.6.1 Size-Dependent Core–Shell Fine Structures

Particle size is an important parameter that strongly influences the activity of catalyst nanoparticles. There are extensive studies on the particle size effect of Pt particles on the ORR catalysis, showing that the area-specific activity increased as the particle size increases due to a lower portion of low-coordinated Pt atoms on the edges and corners [13, 74–77]. Taking the surface area into account, this leads to a maximum mass activity at particle size of around 3–5 nm. Similar trends were also reported in Pt_3M alloy catalysts [13, 78, 79]. For dealloyed nanoparticles, situation becomes more complex as the morphologies and core–shell structures were found to be dependent on the particle size, being an additional contribution to the overall size effect.

Oezaslan et al. found that there were three distinctly different size-dependent morphology regimes in dealloyed $PtCu_3$ and $PtCo_3$ particles, as illustrated in Fig. 18.13 [69]. When smaller than 10 nm, the dealloyed particles generally showed a simple core–shell structure. When the size was between 10 and 20 nm, the dealloyed particles showed more complex core/shell structure, where the Co-/Cu-rich regions split into multiple separate core regions, indicating a near-surface enrichment of Co/Cu. At even larger sizes (greater than 30 nm), surface pits and nanopores coexisting with multiple cores were formed. The appearance of porous dealloyed $PtCu_3$/$PtCo_3$ nanoparticle at larger particle size is also shown in other reports, although the detailed critical sizes may be different [65]. The uncovered size-dependent morphology seems to be general in a wide range of dealloyed

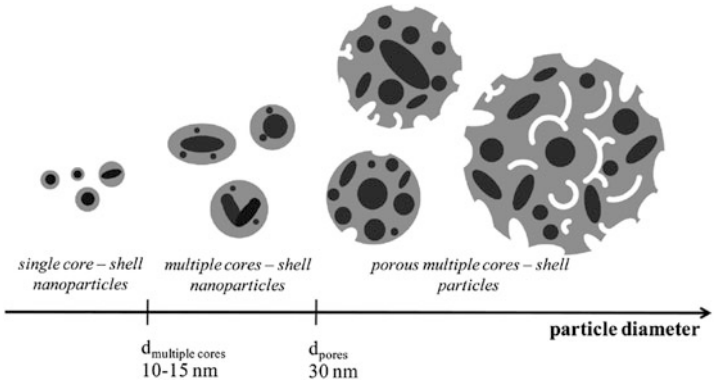

Fig. 18.13 Illustration of the evolution of size-dependent morphology and core–shell fine structures of dealloyed $PtCu_3$ and $PtCo_3$ nanoparticle catalysts (reprint with permission from ref. [69])

Pt nanoparticles. In monodisperse dealloyed $PtNi_3$ nanoparticles, Snyder et al. found that particles with a size greater than approximately 15 nm tended to form nanoporous structure, while particles smaller than 15 nm generally showed nonporous structure [80].

The observed size-dependent morphology of the dealloyed nanoparticle provides an important insight into the existing material gap between dealloyed nanoparticles and highly porous bulk-like bimetallic particles in corrosion science as we previously discussed. The occurrence of porous particles at larger sizes can be explained well from an atomic-scale description of the dealloying process [30, 36, 37]. In larger particles or even bulk bimetallic alloys, diffusion of residual more noble atoms along the extended surface is relatively slow, which results in Rayleigh surface instabilities promoting the formation of nanoporosity. In contrast, in small enough alloy nanoparticles, the lower average coordination of the noble-metal atoms on the surface increases their surface diffusion rate, suppressing the formation of porosity and leading to solid core–shell nanoparticles.

It is still unclear that which kind of core–shell structure contributes the most to the macroscopic overall catalytic activities of the dealloyed catalyst particle ensemble. Researchers at General Motors found that the single-core–shell nanoparticles provided most of the activity for dealloyed $PtCu_3$ catalyst [3], while Snyder et al. found that nanoporous dealloyed $PtNi_3$ particles exhibited higher mass activity and specific activity compared to the dealloyed solid nanoparticles $PtNi_3$ with smaller sizes [80]. Further studies are needed to clarify this issue.

18.6.2 Composition-Dependent Core–Shell Fine Structures

As previously shown in Sect. 18.3.2, the initial compositions of the precursor alloy nanoparticles have a great influence on the activities of the dealloyed nanoparticles.

A higher initial content of the transition metals is expected to result in a higher extent of compressive strain over the formed Pt shell and hence possibly higher ORR activity.

Recently, atomic-scale STEM analysis revealed more complex effects of the initial composition on the core–shell fine structures of dealloyed nanoparticles. By STEM/EDX analysis of a series of $Pt_{1-x}Ni_x$ nanoparticles (Pt_3Ni to $PtNi_3$), Wang et al. found that a higher initial Ni composition resulted in a higher extent of dissolution of Ni atoms, which resulted in a larger Pt-shell thickness [56] (Fig. 18.14). As the strain energy cost would increase with the Pt-shell thickness, there must be a strain relaxation over the shell-thickness direction, leading to a lower extent of the compressive strain on the outmost Pt surface and thus lower ORR activities. Very recently, STEM/EELS studies found that at further larger initial composition, the Pt-shell thickness decreased again [53]. Apart from the different Pt-shell thickness, an unusual Ni-enriched inner shell at subsurface layers was also uncovered in the dealloyed Pt_xNi_{1-x} nanoparticles with higher initial Ni compositions. The composition and the location of the Ni-enriched inner shells are strongly dependent on the initial composition, which further controls the degree of the surface lattice strain and hence the ORR activity of the Pt shell. Therefore, the composition-dependent activity is controlled by a combined effect of Pt-shell thickness and compositional distributions from the subsurface layers to the particle core.

18.6.3 Atomic-Scale Mechanisms of Catalyst Instability

As described in Sect. 18.5, dealloyed Pt catalysts suffered from activity degradation during long-term potential cycling. Both particle growth and dissolution of less-noble transition metals after the potential cycling were confirmed by TEM and EDX analysis. The particle growth was likely caused by a similar instability mechanism as that for Pt, i.e., Ostwald ripening and coalescence, which would lead to a lower surface area. The dissolution of the transition metals would lower down the lattice-strain effect and hence the specific activity. The extent of the dissolution can be dependent on the nature of the transition metals. For instance, dealloyed $PtCu_3$ catalyst exhibited higher Cu content ($Pt_{66}Cu_{34}$) after 10,000 potential cycles compared to dealloyed $PtCo_3$, which changed to $Pt_{83}Co_{17}$ [48]. The higher residual content of Cu can help maintain the lattice strain on the Pt shell and hence results in higher stability. This result suggests that a rational selection of the transition metals is important to achieve high catalyst stability.

Using aberration-corrected STEM and EELS mapping, Xin et al. performed a statistical analysis of elemental distributions in hundreds of Pt_3Co nanoparticles across different stages of catalyst aging in PEMFCs, revealing a surprising coupling among different instability mechanisms (Co leaching, Ostwald ripening, and particle coalescence) [68]. The Pt_3Co catalyst was chemically leached from a PtCo

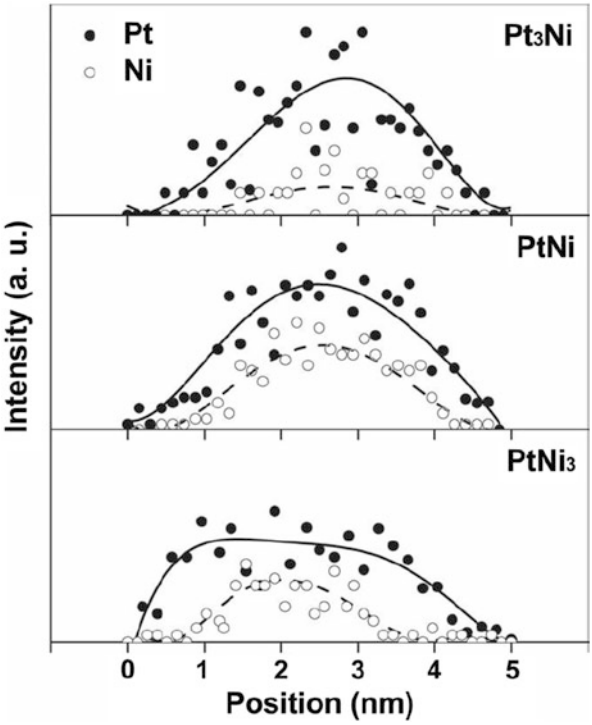

Fig. 18.14 Aberration-corrected STEM and EDX line scan analysis of the core–shell fine structures of dealloyed $Pt_{1-x}Ni_x$ nanoparticles (reprint with permission from ref. [56])

precursor alloy and exhibited single-core–shell structure with a uniform Pt-shell thickness of around 0.7 nm (~3 monolayers). After 30,000 cycles between 0.6 and 1.0 V in a fuel cell MEA, core–shell features were clearly disclosed besides the apparent particle coarsening: firstly, unlike single-core–shell particles before stability test, multiple alloy cores were found in many particles with more complex shape after long-term potential cycling, showing a signature of significant particle coalescence. Such particle coalescence was further clearly visualized by 3-D electron tomography [72]. Secondly, much thicker Pt shells were found, and the larger the particles, the larger the Pt-shell thickness. Interestingly, the increased Pt-shell thickness was found to originate from Pt redeposition through Ostwald ripening instead of Co dissolution. The Co dissolution was suspected to be from smaller particles that had dissolved completely. This is consistent with the Ostwald ripening mechanism, that is, the preferential dissolution of Pt atoms in smaller particles exposed subsurface Co to be co-dissolved, while redeposition of Pt atoms on larger particles protected their Co-containing cores and resulted in thicker Pt shell. Finally, the coalescent multi-core particles exhibited not only larger particle size but also much larger Pt-shell thickness compared to single-core nanoparticles. This may be because there were more Pt redeposition on the irregular coalescent particles to minimum the surface curvature, suggesting a complex

interplay between coalescence and Ostwald ripening mechanism. The thickening of Pt shell especially at larger particles after long-term potential cycling was further confirmed by Carlton et al. [66].

The increased Pt-shell thickness associated with Pt redeposition due to the Ostwald ripening provides a new insight on the instability mechanisms for dealloyed Pt-bimetallic catalyst. Apart from the particle growth that leads to a lowered specific surface area during the Ostwald ripening, the increased Pt-shell thickness gradually relaxed the lattice strain and is a critical reason for the activity degradation. The uncovered Pt-shell thickening due to Ostwald ripening suggests that durability of the catalysts can be further improved through advance in the synthesis of monodisperse nanoparticles. Further studies are also needed to investigate the relative contribution of Pt redeposition and transition-metal dissolution to the increased Pt-shell thickness.

18.7 Conclusion

We have reviewed the family of dealloyed Pt-based nanoparticle electrocatalysts for the electroreduction of oxygen at PEMFC cathodes, which were synthesized by selective dissolution of less-noble atoms from Pt alloy nanoparticle precursors. The dealloyed $PtCu_3$ catalyst showed a promising improvement factor of 4–6 times on the Pt-mass ORR activity compared to a state-of-the-art Pt catalyst. The highly active dealloyed Pt catalysts can be implemented inside a realistic MEA of PEMFCs, where an in situ voltammetric dealloying procedure was used to constructed catalytically active nanoparticles. The core-shell structural character of the dealloyed nanoparticles was confirmed by advanced STEM and elemental line profile analysis. The lattice-contracted transition-metal-rich core resulted in a compressive lattice strain in the Pt-rich shell, which, in turn, favorably modified the chemisorption energies and resulted in improved ORR kinetics.

The dealloyed core–shell nanoparticle concept was successfully extended to a wide range of transition-metal-rich Pt bimetallics ($PtCo_3$ and $PtNi_3$) and Pt trimetallics (Pt–Co–Cu, Pt–Ni–Cu, Pt–Ni–Co, etc.), demonstrating a general strategy to modify the surface catalytic properties of noble metals. Stability tests showed that dealloyed Pt catalysts could in principle maintain their high ORR activities over extended period. However, long-term stability is still a critical challenge. To solve this problem, developing dealloyed Pt-ternary catalysts shows to be a promising way.

Thanks to the advanced characterization techniques such as aberration-corrected electron microscopy and spectroscopy, more complex core–shell fine structures of the dealloyed nanoparticles can be studied at atomic scale [53, 73], enabling a comprehensive understanding on the structure–activity–stability relationship. To achieve both high activity and stability, future works will concentrate on understanding and optimizing the core–shell fine structures of dealloyed nanoparticles through the control of particle size, composition and shape, the dealloying conditions, etc.

Acknowledgments We thank Dr. Marc Heggen for continuing support in advanced electron microscopy. We also thank the Zentraleinrichtung für Elektronenmikroskopie (Zelmi) of the Technical University Berlin for their support with TEM and EDS techniques. LG thanks Dr. Rong Yu and Prof. Jing Zhu for their previous instructions. PS thanks Dr. Shirlaine Koh, Dr. Chengfei Yu, Dr. Ratndeep Srivastava, Dr. Prasanna Mani, Dr. Zengcai Liu, and Dr. Mehtap Oezaslan for their support over the past years. PS acknowledges financial support through the Cluster of Excellence in Catalysis (UniCat) funded by DFG and managed by TU Berlin.

References

1. Gasteiger HA, Kocha SS, Sompalli B, Wagner FT (2005) Activity benchmarks and requirements for pt, pt-alloy, and non-pt oxygen reduction catalysts for PEMFCs. Appl Catal B Environ 56(1–2):9–35
2. Gasteiger HA, Markovic NM (2009) Just a dream-or future reality? Science 324(5923):48–49
3. Wagner FT, Lakshmanan B, Mathias MF (2010) Electrochemistry and the future of the automobile. J Phys Chem Lett 1(14):2204–2219
4. Debe MK (2012) Electrocatalyst approaches and challenges for automotive fuel cells. Nature 486(7401):43–51
5. Bashyam R, Zelenay P (2006) A class of non-precious metal composite catalysts for fuel cells. Nature 443(7107):63–66
6. Lefevre M, Proietti E, Jaouen F, Dodelet JP (2009) Iron-based catalysts with improved oxygen reduction activity in polymer electrolyte fuel cells. Science 324(5923):71–74
7. Wu G, More KL, Johnston CM, Zelenay P (2011) High-performance electrocatalysts for oxygen reduction derived from polyaniline, iron, and cobalt. Science 332(6028):443–447
8. Li Y, Zhou W, Wang H, Xie L, Liang Y, Wei F, Idrobo J-C, Pennycook SJ, Dai H (2012) An oxygen reduction electrocatalyst based on carbon nanotube-graphene complexes. Nat Nanotechnol 7(6):394–400
9. Stamenkovic V, Mun BS, Mayrhofer KJJ, Ross PN, Markovic NM, Rossmeisl J, Greeley J, Norskov JK (2006) Changing the activity of electrocatalysts for oxygen reduction by tuning the surface electronic structure. Angew Chem Int Ed 45(18):2897–2901
10. Greeley J, Stephens IEL, Bondarenko AS, Johansson TP, Hansen HA, Jaramillo TF, Rossmeisl J, Chorkendorff I, Norskov JK (2009) Alloys of platinum and early transition metals as oxygen reduction electrocatalysts. Nat Chem 1(7):552–556
11. Zhang JL, Vukmirovic MB, Xu Y, Mavrikakis M, Adzic RR (2005) Controlling the catalytic activity of platinum-monolayer electrocatalysts for oxygen reduction with different substrates. Angew Chem Int Ed 44(14):2132–2135
12. Toda T, Igarashi H, Uchida H, Watanabe M (1999) Enhancement of the electroreduction of oxygen on pt alloys with Fe, Ni, and Co. J Electrochem Soc 146(10):3750–3756
13. M-k M, Cho J, Cho K, Kim H (2000) Particle size and alloying effects of Pt-based alloy catalysts for fuel cell applications. Electrochim Acta 45(25–26):4211–4217
14. Paulus UA, Wokaun A, Scherer GG, Schmidt TJ, Stamenkovic V, Radmilovic V, Markovic NM, Ross PN (2002) Oxygen reduction on carbon-supported Pt-Ni and Pt-Co alloy catalysts. J Phys Chem B 106(16):4181–4191
15. Salgado JRC, Antolini E, Gonzalez ER (2004) Structure and activity of carbon-supported Pt-Co electrocatalysts for oxygen reduction. J Phys Chem B 108(46):17767–17774
16. Yang H, Alonso-Vante N, Leger JM, Lamy C (2004) Tailoring, structure, and activity of carbon-supported nanosized Pt-Cr alloy electrocatalysts for oxygen reduction in pure and methanol-containing electrolytes. J Phys Chem B 108(6):1938–1947

17. Yang H, Vogel W, Lamy C, Alonso-Vante N (2004) Structure and electrocatalytic activity of carbon-supported Pt-Ni alloy nanoparticles toward the oxygen reduction reaction. J Phys Chem B 108(30):11024–11034
18. Zhang J, Mo Y, Vukmirovic MB, Klie R, Sasaki K, Adzic RR (2004) Platinum monolayer electrocatalysts for O_2 reduction: Pt monolayer on Pd(111) and on carbon-supported Pd nanoparticles. J Phys Chem B 108(30):10955–10964
19. Zhang J, Lima FHB, Shao MH, Sasaki K, Wang JX, Hanson J, Adzic RR (2005) Platinum monolayer on nonnoble metal-noble metal core-shell nanoparticle electrocatalysts for O_2 reduction. J Phys Chem B 109(48):22701–22704
20. Zhang JL, Vukmirovic MB, Sasaki K, Nilekar AU, Mavrikakis M, Adzic RR (2005) Mixed-metal Pt monolayer electrocatalysts for enhanced oxygen reduction kinetics. J Am Chem Soc 127(36):12480–12481
21. Adzic RR, Zhang J, Sasaki K, Vukmirovic MB, Shao M, Wang JX, Nilekar AU, Mavrikakis M, Valerio JA, Uribe F (2007) Platinum monolayer fuel cell electrocatalysts. Top Catal 46 (3–4):249–262
22. Zhang J, Sasaki K, Sutter E, Adzic RR (2007) Stabilization of platinum oxygen-reduction electrocatalysts using gold clusters. Science 315(5809):220–222
23. Wang JX, Inada H, Wu LJ, Zhu YM, Choi YM, Liu P, Zhou WP, Adzic RR (2009) Oxygen reduction on well-defined core-shell nanocatalysts: particle size, facet, and pt shell thickness effects. J Am Chem Soc 131(47):17298–17302
24. Stamenkovic VR, Mun BS, Mayrhofer KJJ, Ross PN, Markovic NM (2006) Effect of surface composition on electronic structure, stability, and electrocatalytic properties of pt-transition metal alloys: Pt-skin versus Pt-skeleton surfaces. J Am Chem Soc 128(27):8813–8819
25. Stamenkovic VR, Fowler B, Mun BS, Wang GF, Ross PN, Lucas CA, Markovic NM (2007) Improved oxygen reduction activity on $Pt_3Ni(111)$ via increased surface site availability. Science 315(5811):493–497
26. Stamenkovic VR, Mun BS, Arenz M, Mayrhofer KJJ, Lucas CA, Wang GF, Ross PN, Markovic NM (2007) Trends in electrocatalysis on extended and nanoscale Pt-bimetallic alloy surfaces. Nat Mater 6(3):241–247
27. Koh S, Strasser P (2007) Electrocatalysis on bimetallic surfaces: modifying catalytic reactivity for oxygen reduction by voltammetric surface dealloying. J Am Chem Soc 129(42):12624–12625
28. Bardal E (2004) Corrosion and protection. Springer, London
29. Raney M (1927) Method of producing finely divided nickel. US Patent 1,628,190
30. Erlebacher J, Aziz MJ, Karma A, Dimitrov N, Sieradzki K (2001) Evolution of nanoporosity in dealloying. Nature 410(6827):450–453
31. Ding Y, Erlebacher J (2003) Nanoporous metals with controlled multimodal pore size distribution. J Am Chem Soc 125(26):7772–7773
32. Ding Y, Chen MW, Erlebacher J (2004) Metallic mesoporous nanocomposites for electrocatalysis. J Am Chem Soc 126(22):6876–6877
33. Ding Y, Kim YJ, Erlebacher J (2004) Nanoporous gold leaf: "ancient technology"/advanced material. Adv Mater 16(21):1897–1900
34. Snyder J, Asanithi P, Dalton AB, Erlebacher J (2008) Stabilized nanoporous metals by dealloying ternary alloy precursors. Adv Mater 20(24):4883–4886
35. Snyder J, Fujita T, Chen MW, Erlebacher J (2010) Oxygen reduction in nanoporous metal-ionic liquid composite electrocatalysts. Nat Mater 9(11):904–907
36. Erlebacher J (2004) An atomistic description of dealloying – porosity evolution, the critical potential, and rate-limiting behavior. J Electrochem Soc 151(10):C614–C626
37. Erlebacher J (2011) Mechanism of coarsening and bubble formation in high-genus nanoporous metals. Phys Rev Lett 106(22):225504
38. Mani P, Srivastava R, Strasser P (2008) Dealloyed Pt-Cu core-shell nanoparticle electrocatalysts for use in PEM fuel cell cathodes. J Phys Chem C 112(7):2770–2778
39. Oezaslan M, Hasche F, Strasser P (2011) In situ observation of bimetallic alloy nanoparticle formation and growth using high-temperature XRD. Chem Mater 23(8):2159–2165

40. Strasser P, Koha S, Greeley J (2008) Voltammetric surface dealloying of Pt bimetallic nanoparticles: an experimental and DFT computational analysis. Phys Chem Chem Phys 10(25):3670–3683
41. Srivastava R, Mani P, Hahn N, Strasser P (2007) Efficient oxygen reduction fuel cell electrocatalysis on voltammetrically dealloyed Pt-Cu-Co nanoparticles. Angew Chem Int Ed 46(47):8988–8991
42. Yu CF, Koh S, Leisch JE, Toney MF, Strasser P (2008) Size and composition distribution dynamics of alloy nanoparticle electrocatalysts probed by anomalous small angle X-ray scattering (ASAXS). Faraday Discuss 140:283–296
43. Strasser P, Koh S, Anniyev T, Greeley J, More K, Yu CF, Liu ZC, Kaya S, Nordlund D, Ogasawara H, Toney MF, Nilsson A (2010) Lattice-strain control of the activity in dealloyed core-shell fuel cell catalysts. Nat Chem 2(6):454–460
44. Hammer B, Norskov JK (1995) Why gold is the noblest of all the metals. Nature 376 (6537):238–240
45. Mavrikakis M, Hammer B, Norskov JK (1998) Effect of strain on the reactivity of metal surfaces. Phys Rev Lett 81(13):2819–2822
46. Wang C, Chi MF, Li DG, van der Vliet D, Wang GF, Lin QY, Mitchell JF, More KL, Markovic NM, Stamenkovic VR (2011) Synthesis of homogeneous pt-bimetallic nanoparticles as highly efficient electrocatalysts. ACS Catal 1(10):1355–1359
47. Mani P, Srivastava R, Strasser P (2011) Dealloyed binary PtM_3 (M = Cu, Co, Ni) and ternary $PtNi_3M$ (M = Cu, Co, Fe, Cr) electrocatalysts for the oxygen reduction reaction: performance in polymer electrolyte membrane fuel cells. J Power Sources 196(2):666–673
48. Hasché F, Oezaslan M, Strasser P (2011) Activity, stability, and degradation mechanisms of dealloyed $PtCu_3$ and $PtCo_3$ nanoparticle fuel cell catalysts. ChemCatChem 3(11):1805–1813
49. Oezaslan M, Strasser P (2011) Activity of dealloyed $PtCo_3$ and $PtCu_3$ nanoparticle electrocatalyst for oxygen reduction reaction in polymer electrolyte membrane fuel cell. J Power Sources 196(12):5240–5249
50. Hasche F, Oezaslan M, Strasser P (2012) Activity, structure and degradation of dealloyed $PtNi_3$/nanoparticle electrocatalyst for the oxygen reduction reaction in PEMFC. J Electrochem Soc 159(1):B25–B34
51. Oezaslan M, Hasche F, Strasser P (2012) Oxygen electroreduction on $PtCo_3$, PtCo and Pt_3Co alloy nanoparticles for alkaline and acidic PEM fuel cells. J Electrochem Soc 159(4): B394–B405
52. Rudi S, Tuaev X, Strasser P (2012) Electrocatalytic oxygen reduction on dealloyed $Pt_{1-x}Ni_x$ alloy nanoparticle electrocatalysts. Electrocatalysis. doi:10.1007/s12678-12012-10098-x
53. Gan L, Heggen M, Rudi S, Strasser P (2012) Core-shell compositional fine structures of dealloyed Pt_xNi_{1-x} nanoparticles and their impact on oxygen reduction catalysis. Nano Lett 12(10):5423–5430
54. Debe MK, Steinbach AJ, Vernstrom GD, Hendricks SM, Kurkowski MJ, Atanasoski RT, Kadera P, Stevens DA, Sanderson RJ, Marvel E, Dahn JR (2011) Extraordinary oxygen reduction activity of Pt_3Ni_7. J Electrochem Soc 158(8):B910–B918
55. Stevens DA, Wang S, Sanderson RJ, Liu GCK, Vernstrom GD, Atanasoski RT, Debe MK, Dahn JR (2011) A combined rotating disk electrode/x-ray diffraction study of co dissolution from $Pt_{1-x}Co_x$ alloys. J Electrochem Soc 158(8):B899–B904
56. Wang C, Chi MF, Wang GF, van der Vliet D, Li DG, More K, Wang HH, Schlueter JA, Markovic NM, Stamenkovic VR (2011) Correlation between surface chemistry and electrocatalytic properties of monodisperse Pt_xNi_{1-x} nanoparticles. Adv Funct Mater 21(1):147–152
57. Liu Y, Hangarter CM, Bertocci U, Moffat TP (2012) Oxygen reduction reaction on electrodeposited $Pt_{100-x}Ni_x$: influence of alloy composition and dealloying. J Phys Chem C 116(14):7848–7862

58. Wanjala BN, Fang B, Luo J, Chen YS, Yin J, Engehard MH, Loukrakpam R, Zhong CJ (2011) Correlation between atomic coordination structure and enhanced electrocatalytic activity for trimetallic alloy catalysts. J Am Chem Soc 133(32):12714–12727
59. Wang C, Li D, Chi M, Pearson J, Rankin RB, Greeley J, Duan Z, Wang G, van der Vliet D, More KL, Markovic NM, Stamenkovic VR (2012) Rational development of ternary alloy electrocatalysts. J Phys Chem Lett 3(12):1668–1673
60. Shao-Horn Y, Sheng W, Chen S, Ferreira P, Holby E, Morgan D (2007) Instability of supported platinum nanoparticles in low-temperature fuel cells. Top Catal 46(3):285–305
61. Mayrhofer KJJ, Hartl K, Juhart V, Arenz M (2009) Degradation of carbon-supported Pt bimetallic nanoparticles by surface segregation. J Am Chem Soc 131(45):16348–16349
62. Neyerlin KC, Srivastava R, Yu CF, Strasser P (2009) Electrochemical activity and stability of dealloyed Pt-Cu and Pt-Cu-Co electrocatalysts for the oxygen reduction reaction (ORR). J Power Sources 186(2):261–267
63. Chen S, Ferreira PJ, Sheng WC, Yabuuchi N, Allard LF, Shao-Horn Y (2008) Enhanced activity for oxygen reduction reaction on "Pt_3Co" nanoparticles: direct evidence of percolated and sandwich-segregation structures. J Am Chem Soc 130(42):13818–13819
64. Chen S, Sheng WC, Yabuuchi N, Ferreira PJ, Allard LF, Shao-Horn Y (2009) Origin of oxygen reduction reaction activity on "Pt_3Co" nanoparticles: atomically resolved chemical compositions and structures. J Phys Chem C 113(3):1109–1125
65. Dutta I, Carpenter MK, Balogh MP, Ziegelbauer JM, Moylan TE, Atwan MH, Irish NP (2010) Electrochemical and structural study of a chemically dealloyed PtCu oxygen reduction catalyst. J Phys Chem C 114(39):16309–16320
66. Carlton CE, Chen S, Ferreira PJ, Allard LF, Shao-Horn Y (2012) Sub-nanometer-resolution elemental mapping of "Pt_3Co" nanoparticle catalyst degradation in proton-exchange membrane fuel cells. J Phys Chem Lett 3(2):161–166
67. Gan L, Yu R, Luo J, Cheng ZY, Zhu J (2012) Lattice strain distributions in individual dealloyed Pt-Fe catalyst nanoparticles. J Phys Chem Lett 3(7):934–938
68. Xin HL, Mundy JA, Liu ZY, Cabezas R, Hovden R, Kourkoutis LF, Zhang JL, Subramanian NP, Makharia R, Wagner FT, Muller DA (2012) Atomic-resolution spectroscopic imaging of ensembles of nanocatalyst particles across the life of a fuel cell. Nano Lett 12(1):490–497
69. Oezaslan M, Heggen M, Strasser P (2012) Size-dependent morphology of dealloyed bimetallic catalysts: linking the nano to the macro scale. J Am Chem Soc 134(1):514–524
70. Haider M, Uhlemann S, Schwan E, Rose H, Kabius B, Urban K (1998) Electron microscopy image enhanced. Nature 392(6678):768–769
71. Urban KW (2008) Studying atomic structures by aberration-corrected transmission electron microscopy. Science 321(5888):506–510
72. Yu Y, Xin HL, Hovden R, Wang D, Rus ED, Mundy JA, Muller DA, Abruña HD (2012) Three-dimensional tracking and visualization of hundreds of Pt−Co fuel cell nanocatalysts during electrochemical aging. Nano Lett 12(9):4417–4423
73. Heggen M, Oezaslan M, Houben L, Strasser P (2012) Formation and analysis of core–shell fine structures in Pt bimetallic nanoparticle fuel cell electrocatalysts. J Phys Chem C 116(36): 19073–19083
74. Yamamoto K, Imaoka T, Chun WJ, Enoki O, Katoh H, Takenaga M, Sonoi A (2009) Size-specific catalytic activity of platinum clusters enhances oxygen reduction reactions. Nat Chem 1(5):397–402
75. Nesselberger M, Ashton S, Meier JC, Katsounaros I, Mayrhofer KJJ, Arenz M (2011) The particle size effect on the oxygen reduction reaction activity of pt catalysts: influence of electrolyte and relation to single crystal models. J Am Chem Soc 133(43):17428–17433
76. Shao MH, Peles A, Shoemaker K (2011) Electrocatalysis on platinum nanoparticles: particle size effect on oxygen reduction reaction activity. Nano Lett 11(9):3714–3719
77. Perez-Alonso FJ, McCarthy DN, Nierhoff A, Hernandez-Fernandez P, Strebel C, Stephens IEL, Nielsen JH, Chorkendorff I (2012) The effect of size on the oxygen electroreduction activity of mass-selected platinum nanoparticles. Angew Chem Int Ed 51(19):4641–4643

78. Wang C, van der Vilet D, Chang KC, You HD, Strmcnik D, Schlueter JA, Markovic NM, Stamenkovic VR (2009) Monodisperse Pt_3Co nanoparticles as a catalyst for the oxygen reduction reaction: size-dependent activity. J Phys Chem C 113(45):19365–19368
79. Wang C, Wang GF, van der Vliet D, Chang KC, Markovic NM, Stamenkovic VR (2010) Monodisperse Pt_3Co nanoparticles as electrocatalyst: the effects of particle size and pretreatment on electrocatalytic reduction of oxygen. Phys Chem Chem Phys 12(26):6933–6939
80. Snyder J, McCue I, Livi K, Erlebacher J (2012) Structure/processing/properties relationships in nanoporous nanoparticles as applied to catalysis of the cathodic oxygen reduction reaction. J Am Chem Soc 134:8633–8645